INTERNATIONAL JOURNAL FOR NUMERICAL METHODS IN FLUIDS
Int. J. Numer. Meth. Fluids 2002; **38**:589–608 (DOI: 10.1002/fld.221)

A simple and efficient error analysis for multi-step solution of the Navier–Stokes equations

R. M. Fithen*

Engineering Department, Arkansas Tech University, Russellville, AR 72801, U.S.A.

SUMMARY

A simple error analysis is used within the context of segregated finite element solution scheme to solve incompressible fluid flow. An error indicator is defined based on the difference between a numerical solution on an original mesh and an approximated solution on a related mesh. This error indicator is based on satisfying the steady-state momentum equations. The advantages of this error indicator are, simplicity of implementation (post-processing step), ability to show regions of high and/or low error, and as the indicator approaches zero the solution approaches convergence. Two examples are chosen for solution; first, the lid-driven cavity problem, followed by the solution of flow over a backward facing step. The solutions are compared to previously published data for validation purposes. It is shown that this rather simple error estimate, when used as a re-meshing guide, can be very effective in obtaining accurate numerical solutions. Copyright © 2002 John Wiley & Sons, Ltd.

KEY WORDS: error analysis; Navier–Stokes; incompressible fluid flow

1. INTRODUCTION

The method chosen to solve the incompressible Navier–Stokes equation is the method presented by Comini and Del Giudice [1, 2] and used later by Kim and Chung [3]. This method has several advantages over direct methods, one major advantage is less computer memory is required to obtain a solution [4]. Another advantage is the Ladyzhenskaya–Babuska–Brezzi (LBB) [5, 6] condition can be relaxed, and an equal interpolation for the velocities and pressure can take place. In this work the method of Comini and Del Giudice [1, 2] and Kim and Chung [3] is compared with that of Dukowicz and Dvinsky [7]. The result of this comparison shows that the method of Comini and Del Giudice is a subset of that presented by Dukowicz and Dvinsky. However, by observing the numerical method based on the derivation of Dukowicz and Dvinsky, clear insight into the nature of the pressure–velocity approximations can be observed. Work is presently being done by Gresho *et al.* [8] addressing inaccuracies in the pressure approximations for these type of methods. Gresho points out that any pressure projection method is limited to time-accurate solutions and is inappropriate for seeking

*Correspondence to: R. M. Fithen, Engineering Department, Arkansas Tech University, Russellville, AR 72801, U.S.A.

Received 5 February 1996
Revised 1 June 2001

steady-state solutions via large time steps. In this paper, a pressure projection method is used to obtain a steady solution via small time steps. However, the error analysis presented in this work is purely based on satisfying the steady-state form of the governing equations.

Error estimation seeks answers to basically two questions. (1) What is the error in the solution at hand (error estimation), and (2) what is the change in the error if we refine our mesh (error indicators)? In this paper only the second form of error analysis is used. In effect, we seek to answer the question 'If we refine the mesh in a particular way, what then is the difference between the two solutions?' In order to answer this question we turn to the work in References [9–11]. The authors suggest a hierarchical approach in which all previously existing basis functions with each element are preserved, and additional basis functions are added. Thus, the added degree of freedom can be viewed as a perturbation within the original solution and, hence, can be used to determine the difference between the two successive solutions. The first non-perturbed solution is obtained in the standard way, while the second solution is obtained by iterating once using the non-perturbed solution as a starting point. In the present work, this type of hierarchical basis function will be used in order to obtain an indicator of the error in the domain.

PROBLEM STATEMENT

Many problems existing in fluid mechanics can be treated as constant property incompressible flows. Some examples include subsonic flow of gases, and flow of most liquids. This class of problems can be solved through the use of the incompressible Navier–Stokes equations.

$$\frac{\partial u}{\partial t} + u\frac{\partial u}{\partial x} + v\frac{\partial u}{\partial y} = f_x - \frac{\partial P}{\partial x} + \frac{1}{Re}\left(\frac{\partial^2 u}{\partial x^2} + \frac{\partial^2 u}{\partial y^2}\right) \tag{1}$$

$$\frac{\partial u}{\partial t} + u\frac{\partial v}{\partial x} + v\frac{\partial v}{\partial y} = f_y - \frac{\partial P}{\partial y} + \frac{1}{Re}\left(\frac{\partial^2 v}{\partial x^2} + \frac{\partial^2 v}{\partial y^2}\right) \tag{2}$$

These equations are derived from a balance of momentum in both the x and y directions. The conservation of mass yields,

$$\frac{\partial u}{\partial x} + \frac{\partial v}{\partial y} = 0 \tag{3}$$

In an incompressible flow situation, the momentum equations must be solved subject to the constraint that the mass must be conserved for all time t. Satisfying this constraint is in fact one of the major ways in which solution techniques have been classified. Solving the continuity constraint while simultaneously satisfying our momentum equations is classified as a mixed method. Solving this constraint through the use of a bulk modulus-type approach is classified as a penalty method,

$$P = -\lambda\left(\frac{\partial u}{\partial x} + \frac{\partial v}{\partial y}\right) \tag{4}$$

where λ is a specified large number. Both the mixed and penalty formulation to incompressible flow problems are presented by Reddy [12]. Solving each of these equations separately such

that at the end of the solution/time step all the equations are satisfied can be classified as a segregated (or fractional step) approach. From observing Equation (4), one can immediately observe a form of the LBB condition. In order for Equation (4) to be exactly satisfied in a discrete sense, the pressure must be of one polynomial order lower than that of the velocity.

For the weak form of the weighted residual methods the boundary conditions depend on how the governing differential equations are weakened. If the boundary is represented as Γ. The following boundary conditions will be applied to a subset of Γ:

1. Essential boundary condition applied to Γ_c

$$\begin{aligned} u &= u_{bc} \\ v &= v_{bc} \end{aligned} \tag{5}$$

2. Natural boundary condition applied to Γ_n

$$\begin{aligned} g_x &= \left(\frac{1}{Re}\frac{\partial u}{\partial x} - p\right) n_x + \left(\frac{1}{Re}\frac{\partial v}{\partial y}\right) n_y \\ g_y &= \left(\frac{1}{Re}\frac{\partial v}{\partial y} - p\right) n_y + \left(\frac{1}{Re}\frac{\partial u}{\partial x}\right) n_x \end{aligned} \tag{6}$$

Where, n_x and n_y are unit normals in the x and y directions normal to the boundaries.

SOLUTION PROCEDURE

The solution procedure represented below is that of Dukowicz and Dvinsky [7]. For fully implicit Navier–Stokes equations, the x and y equations may be represented in a matrix operator form as:

$$[\mathscr{M}](u^{n+1} - u^n) - \Delta t[\mathscr{K}]u^{n+1} + \Delta t[\mathscr{C}^x]p^{n+1} = \Delta t\{\mathscr{F}_x\}^{n+1} \tag{7}$$

$$[\mathscr{M}](v^{n+1} - v^n) - \Delta t[\mathscr{K}]v^{n+1} + \Delta t[\mathscr{C}^y]p^{n+1} = \Delta t\{\mathscr{F}_y\}^{n+1} \tag{8}$$

The Continuity equation can be represented through finite elements as:

$$[\mathscr{C}^x]^T u^{n+1} + [\mathscr{C}^y]^T v^{n+1} = \{0\} \tag{9}$$

Where,

$[\mathscr{M}]$ is the discrete form of the mass matrix,
$[\mathscr{K}]$ is the discrete form of the convective and diffusive portions of the Navier–Stokes equations,
$[\mathscr{C}^x]$ is the discrete form of the x component of gradient matrix,
$[\mathscr{C}^y]$ is the discrete form of the y component of gradient matrix,
$[\mathscr{C}^x]^T$ is the discrete form of the x component of divergence matrix,
$[\mathscr{C}^y]^T$ is the discrete form of the y component of divergence matrix,
$\{\mathscr{F}\}$ is the right hand side to the Navier–Stokes equations, containing the boundary conditions,

These three equations can be represented in full matrix form as:

$$\begin{bmatrix} [\mathscr{M}]-\Delta t[\mathscr{K}] & 0 & \Delta t[\mathscr{C}^x] \\ 0 & [\mathscr{M}]-\Delta t[\mathscr{K}] & \Delta t[\mathscr{C}^y] \\ [\mathscr{C}^x]^T & [\mathscr{C}^y]^T & 0 \end{bmatrix} \begin{Bmatrix} u^{n+1} \\ v^{n+1} \\ \delta p^{n+1} \end{Bmatrix}$$

$$= \begin{bmatrix} [\mathscr{M}] & 0 & -\Delta t[\mathscr{C}^x] \\ 0 & [\mathscr{M}] & -\Delta t[\mathscr{C}^y] \\ 0 & 0 & 0 \end{bmatrix} \begin{Bmatrix} u^n \\ v^n \\ p^n \end{Bmatrix} + \Delta t \begin{Bmatrix} \{\mathscr{F}_x\}^{n+1} \\ \{\mathscr{F}_y\}^{n+1} \\ \{0\} \end{Bmatrix} \tag{10}$$

Where, $\delta p^{n+1} = p^{n+1} - p^n$. In order to solve this system of equations for the velocities and pressures at the next time step, the left hand matrix should be inverted. If one chooses to pursue this approach, there will be several problems encountered. First, the LBB condition must be satisfied. Also, pivoting must be reformed in the inversion due to zeros on the diagonals of the matrix to invert. This type of approach is commonly called a time dependent mixed formulation [12]. If instead of inverting this matrix we look for an approximately factorized form, we can significantly reduce the work load required to solve this system. Following the work of Dukowicz and Dvinsky [7] we develop an approximately factorized form of the matrix,

$$\begin{bmatrix} [\mathscr{M}]-\Delta t[\mathscr{K}] & 0 & \Delta t[\mathscr{C}^x] \\ 0 & [\mathscr{M}]-\Delta t[\mathscr{K}] & \Delta t[\mathscr{C}^y] \\ [\mathscr{C}^x]^T & [\mathscr{C}^y]^T & 0 \end{bmatrix}$$

$$\approx \begin{bmatrix} [\mathscr{M}]-\Delta t[\mathscr{K}] & 0 & 0 \\ 0 & [\mathscr{M}]-\Delta t[\mathscr{K}] & 0 \\ 0 & 0 & [I] \end{bmatrix}$$

$$\times \begin{bmatrix} [I] & 0 & \Delta t[\mathscr{M}]^{-1}[\mathscr{C}^x] \\ 0 & [I] & \Delta t[\mathscr{M}]^{-1}[\mathscr{C}^y] \\ [\mathscr{C}^x]^T & [\mathscr{C}^y]^T & -\Delta t\left[[\mathscr{L}]-[\mathscr{C}^x]^T[\mathscr{M}]^{-1}[\mathscr{C}^x]-[\mathscr{C}^y]^T[\mathscr{M}]^{-1}[\mathscr{C}^y]\right] \end{bmatrix} \tag{11}$$

Where, $[\mathscr{L}]$ is the Laplacian operator in finite element form. As usual with the approximate factorization methods, these equations are separated and solved in two solution steps.

$$\begin{bmatrix} [\mathscr{M}]-\Delta t[\mathscr{K}] & 0 & 0 \\ 0 & [\mathscr{M}]-\Delta t[\mathscr{K}] & 0 \\ 0 & 0 & [I] \end{bmatrix} \begin{Bmatrix} u^* \\ v^* \\ \mathscr{Z} \end{Bmatrix}$$

$$= \begin{bmatrix} [\mathscr{M}] & 0 & -\Delta t[\mathscr{C}^x] \\ 0 & [\mathscr{M}] & -\Delta t[\mathscr{C}^y] \\ 0 & 0 & 0 \end{bmatrix} \begin{Bmatrix} u^n \\ v^n \\ p^n \end{Bmatrix} + \Delta t \begin{Bmatrix} \{\mathscr{F}_x\}^{n+1} \\ \{\mathscr{F}_y\}^{n+1} \\ 0 \end{Bmatrix} \tag{12}$$

followed by:

$$\begin{bmatrix} [I] & 0 & \Delta t[\mathscr{M}]^{-1}[\mathscr{C}^x] \\ 0 & [I] & \Delta t[\mathscr{M}]^{-1}[\mathscr{C}^y] \\ [\mathscr{C}^x]^T & [\mathscr{C}^y]^T & -\Delta t\left[[\mathscr{L}] - [\mathscr{C}^x]^T[\mathscr{M}]^{-1}[\mathscr{C}^x] - [\mathscr{C}^y]^T[\mathscr{M}]^{-1}[\mathscr{C}^y]\right] \end{bmatrix} \begin{Bmatrix} u^{n+1} \\ v^{n+1} \\ \delta p^{n+1} \end{Bmatrix} = \begin{Bmatrix} u^* \\ v^* \\ \mathscr{Z} \end{Bmatrix} \tag{13}$$

Where $\mathscr{Z}$ is the null vector obtained from Equation (12). In order to solve Equation (13), the matrix equation must be changed into a similar set of matrix equations by performing the following matrix operations.

Row (3) = Row (3) – $[\mathscr{C}^x]^T \times$ Row (1)–$[\mathscr{C}^y]^T \times$ Row (2).
Row (1) = $[\mathscr{M}] \times$ Row (1).
Row (2) = $[\mathscr{M}] \times$ Row (2).

Upon performing the basic matrix operations, one obtains:

$$\begin{bmatrix} [\mathscr{M}] & 0 & \Delta t[\mathscr{C}^x] \\ 0 & [\mathscr{M}] & \Delta t[\mathscr{C}^y] \\ 0 & 0 & \Delta t[\mathscr{L}] \end{bmatrix} \begin{Bmatrix} u^{n+1} \\ v^{n+1} \\ \delta p^{n+1} \end{Bmatrix} = \begin{Bmatrix} [\mathscr{M}]u^* \\ [\mathscr{M}]v^* \\ [\mathscr{C}^x]^T u^* + [\mathscr{C}^y]^T v^* \end{Bmatrix} \tag{14}$$

Breaking matrix Equations (12) and (14) apart into components, we obtain the following solution sequence:

Step 1: Guess a pressure distribution p^n
Step 2: Solve the momentum equations

$$[[\mathscr{M}] - \Delta t[\mathscr{K}]]\, u^* = [\mathscr{M}]u^n - \Delta t[\mathscr{C}^x]\, p^n + \Delta t\{\mathscr{F}_x\} \tag{15}$$

$$[[\mathscr{M}] - \Delta t[\mathscr{K}]]\, v^* = [\mathscr{M}]v^n - \Delta t[\mathscr{C}^y]\, p^n + \Delta t\{\mathscr{F}_y\} \tag{16}$$

Step 3: Solve for the pressure correction which will enforce continuity

$$[\mathscr{L}]\delta p^{n+1} = \frac{1}{\Delta t}\left[[\mathscr{C}^x]^T u^* + [\mathscr{C}^y]^T v^*\right] \tag{17}$$

Step 4: Update velocities and pressures

$$[\mathscr{M}]u^{n+1} = [\mathscr{M}]u^* - \Delta t[\mathscr{C}^x]\delta p^{n+1} \tag{18}$$

$$[\mathscr{M}]v^{n+1} = [\mathscr{M}]v^* - \Delta t[\mathscr{C}^y]\delta p^{n+1} \tag{19}$$

$$p^{n+1} = \delta p^{n+1} + p^n \tag{20}$$

Step 6: Test for convergence, if not converged then, return to Step 2.

This formulation is exactly that presented by Comini and Del Guidice [1]. This formulation is also very close in concept to that of the SIMPLE formulations of Patankar [13].

Since an approximate factorization method never gives back the original matrix, it is very instructive to observe what matrix is actually being solved through this formulation. Multiplying out Equation (11) gives some interesting insight into this method of solving the incompressible Navier–Stokes equations. Multiply out this factorization from Equation (11) the left hand side matrix becomes:

$$\begin{bmatrix} [\mathscr{M}] - \Delta t[\mathscr{K}] & 0 & \Delta t[\mathscr{C}^x] - \Delta t^2[\mathscr{K}][\mathscr{M}]^{-1}[\mathscr{C}^x] \\ 0 & [\mathscr{M}] - \Delta t[\mathscr{K}] & \Delta t[\mathscr{C}^y] - \Delta t^2[\mathscr{K}][\mathscr{M}]^{-1}[\mathscr{C}^y] \\ [\mathscr{C}^x]^T & [\mathscr{C}^y]^T & -\Delta t\left[[\mathscr{L}] - [\mathscr{C}^x]^T[\mathscr{M}]^{-1}[\mathscr{C}^x] - [\mathscr{C}^y]^T[\mathscr{M}]^{-1}[\mathscr{C}^y]\right] \end{bmatrix} \tag{21}$$

Using this segregated solution method, the actual equations to be solved are not the discrete Navier–Stokes equations, but are an approximation of the discrete Navier–Stokes equations. Several interesting items may be observed at this point. First, as $[\mathscr{L}]$ approaches the discrete laplacian operator, $[\mathscr{C}^x]^T[\mathscr{M}]^{-1}[\mathscr{C}^x] + [\mathscr{C}^y]^T[\mathscr{M}]^{-1}[\mathscr{C}^y]$, the pressure contribution to the continuity equation becomes lower. In the limit, the continuity becomes undisturbed and may be exactly satisfied (in a finite element sense). However, there are still many unanswered questions about the exact form of the pressure boundary condition and, in fact, this is an area of ongoing research. The extra terms in the momentum equations will never go to zero unless Δt becomes zero. Hence, the Navier–Stokes equations have in a sense become corrupted. One may argue that this in fact is of no consequence since, as p^{n+1} approaches p^n this term approaches zero. However, in solving a steady-state problem one must use this unsteady analysis to converge to a steady solution. In the transient analysis, errors may be introduced that may in fact corrupt the steady-state solution unless Δt is sufficiently small [8]. If this approximate factorization method is used to seek out the steady-state solution to Navier–Stokes equation, the time step should be small enough such that terms like; $\Delta l^2[\mathscr{K}][\mathscr{M}]^{-1}[\mathscr{C}^x]$ are very small. If this is true, the unsteady solution will be time-accurate thereby yielding a steady solution (if one exists).

The elemental level components of the matrices are defined as follows (using index notation):

$$\mathscr{M}_{ij} = \int_\Omega \Psi_i \Psi_j \, \mathrm{d}\Omega \tag{22}$$

$$\mathscr{L}_{ij} = \int_\Omega \left(\frac{\partial \Psi_i}{\partial x}\frac{\partial \Psi_j}{\partial x} + \frac{\partial \Psi_i}{\partial y}\frac{\partial \Psi_j}{\partial y} \right) \mathrm{d}\Omega \tag{23}$$

$$\mathscr{C}^x_{ij} = \int_\Omega \frac{\partial \Psi_i}{\partial x} \Psi_j \, \mathrm{d}\Omega \tag{24}$$

$$\mathscr{C}^y_{ij} = \int_\Omega \frac{\partial \Psi_i}{\partial y} \Psi_j \, \mathrm{d}\Omega \tag{25}$$

$$\mathscr{K}^l_{ij} = \frac{1}{Re} \int_\Omega \left(\frac{\partial \Psi_i}{\partial x}\frac{\partial \Psi_j}{\partial x} + \frac{\partial \Psi_i}{\partial y}\frac{\partial \Psi_j}{\partial y} \right) \mathrm{d}\Omega \tag{26}$$

$$\mathscr{K}^{nl}_{ij} = \int_\Omega \Psi_i \left(u^{-n}\frac{\partial \Psi_j}{\partial x} + v^{-n}\frac{\partial \Psi_j}{\partial y} \right) \mathrm{d}\Omega \tag{27}$$

$$\mathscr{K}_{ij} = \mathscr{K}_{ij}^{nl} + \mathscr{K}_{ij}^{l} \tag{28}$$

$$\mathscr{F}_i^x = \int_\Gamma \Psi_i \left\{ \left(\frac{\partial u}{\partial x} - p \right) n_x + \frac{\partial u}{\partial y} n_y \right\} \mathrm{d}\Gamma \tag{29}$$

$$\mathscr{F}_i^y = \int_\Gamma \Psi_i \left\{ \left(\frac{\partial v}{\partial y} - p \right) n_y + \frac{\partial v}{\partial x} n_x \right\} \mathrm{d}\Gamma \tag{30}$$

These elemental matrices must be combined to form the global system matrices. This combination is processed in such a way as to force a continuous solution over the entire solution domain [12].

FINITE-ELEMENT FORMULATION

As in the case of general element the overall domain is divided into small subdomains (elements) and a basis function over each particular subdomain is generated. The chosen element is triangular and the chosen basis functions can represent any linear function over that triangle. There are actually four basis functions applied over the domain three of the general type and one hierarchical type. These four are shown in Figure 1. The first three basis functions are simply the basis functions from the well-known constant strain triangles. The fourth basis function is of a hierarchical nature and is composed of three composite linear triangles which all equal one at the centroid of the major triangle, and equal zero everywhere on the edges of the major triangle. Although this fourth basis function will not be used within the solution, it will be used to answer one simple question. What will be the effect of breaking every triangle

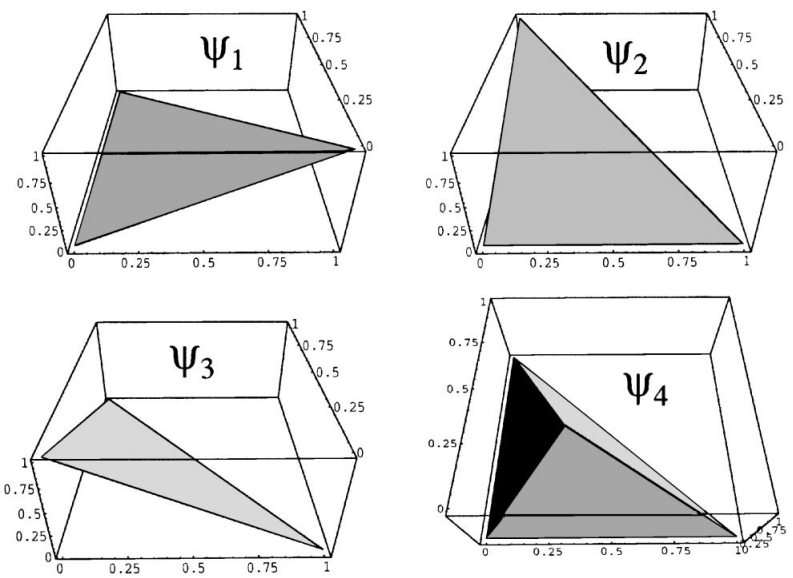

Figure 1. Element basis functions.

in the domain into three triangles each contained with the original triangles and each sharing a common point at the original triangles centroid? With these basis functions a solution to the Navier–Stokes equations will take the form:

$$u = \sum_{e=1}^{N} \left(\sum_{i=1}^{3} \Psi_i^e u_i + \Psi_4^e \delta u_4^e \right) \tag{31}$$

$$v = \sum_{e=1}^{N} \left(\sum_{i=1}^{3} \Psi_i^e v_i + \Psi_4^e \delta v_4^e \right) \tag{32}$$

$$P = \sum_{e=1}^{N} \left(\sum_{i=1}^{3} \Psi_i^e P_i + \Psi_4^e \delta P_4^e \right) \tag{33}$$

Here δu_4^e, δv_4^e and δP_4^e, represent the perturbation in the solution at the centroid of the element e. The general solution proceeds in the following manner. We first select a space $\mathscr{R}$ spanned by a set of basis functions of the form, Ψ_i^e, where $i = 1, 2, 3$ and $e = 1, 2, 3 \ldots N$ ($N =$ number of elements). The space $\mathscr{R}$ is a subspace of $\mathscr{S}$, which is spanned by the set of basis functions, Ψ_i^e, where $i = 1, 2, 3, 4$ and $e = 1, 2, 3 \ldots N$ ($N =$ number of elements). Stepping into the space $\mathscr{R}$, we can represent all functions as a linear combination of the Ψ_i^es contained within $\mathscr{R}$. Using a weighted residual method we determine the coefficients of this linear combination which in the present context are nodal values of the dependent variables. The steps taken up to this point are those of the standard finite element method. It is from this point we diverge in our thought process to obtain error indicators. We now construct a solution from space $\mathscr{S}$ using the Ψ_i^es as basis functions. Using the weighted residual method as before to develop the system matrices, we stop short of solving these equations, and examine the matrices. The global set of equations can be represented as,

$$\begin{bmatrix} [K_{\mathscr{R}}] & [K_{\mathscr{R}\mathscr{S}}] \\ [K_{\mathscr{S}\mathscr{R}}] & [K_{\mathscr{S}}] \end{bmatrix} \begin{Bmatrix} \{a_{\mathscr{R}}\} \\ \{a_{\mathscr{S}}\} \end{Bmatrix} = \begin{Bmatrix} \{F_{\mathscr{R}}\} \\ \{F_{\mathscr{S}}\} \end{Bmatrix} \tag{34}$$

This formulation of error analysis is similar to that presented by the authors of References [9–11]. Observing this equation we see that the original global stiffness matrix $[K_{\mathscr{R}}]$ is embedded within the matrix, and the solution $\{a_{\mathscr{R}}\}$ is also intact. We now seek an approximate solution to $\{a_{\mathscr{S}}\}$ which can be obtained in one step as,

$$\{a_{\mathscr{S}}\} = [K_{\mathscr{S}}]^{-1}\{F_{\mathscr{S}}\} - [K_{\mathscr{S}}]^{-1}[K_{\mathscr{S}\mathscr{R}}]\{a_{\mathscr{R}}\} \tag{35}$$

One very important observation can be made at this point. The fourth degree of freedom in each element is associated with an internal node, hence no other element within the mesh will contain this node. This effectively makes the error analysis an element-by-element process and the global matrix need not be assembled. In order to obtain a more clear understanding we pick a representative element, and construct the u-momentum equation,

$$\begin{bmatrix} \hat{K}_{11} & \hat{K}_{12} & \hat{K}_{13} & \hat{K}_{14} \\ \hat{K}_{21} & \hat{K}_{22} & \hat{K}_{23} & \hat{K}_{24} \\ \hat{K}_{31} & \hat{K}_{32} & \hat{K}_{33} & \hat{K}_{34} \\ \hat{K}_{41} & \hat{K}_{42} & \hat{K}_{43} & \hat{K}_{44} \end{bmatrix} \begin{Bmatrix} u_1 \\ u_2 \\ v_3 \\ \delta v_4^e \end{Bmatrix} = \begin{Bmatrix} Q_1^x \\ Q_2^x \\ Q_3^x \\ Q_4^x \end{Bmatrix} \tag{36}$$

where

$$\hat{K}_{ij} = \mathcal{K}_{ij}^{nl} + \frac{1}{Re}\mathcal{K}_{ij}^{l} \tag{37}$$

$$Q_i^x = \mathcal{F}_i^x - \mathcal{C}_{ij}^x p_j \tag{38}$$

One may notice at this point the stiffness matrix and force vector are not the same as in Step 2 of our solution process. If the equations in Step 2 are divided by Δt and the limit is taken as $\Delta t \to \infty$, we obtain the stiffness matrix and force vector associated with the steady-state form of the momentum equations, the solution to which we seek. Based on this argument the original solution obtained within the context of standard finite element method should be converged in time before this error analysis can effectively take place. Seeking an approximation to the fourth degree of freedom within each element we obtain,

$$\delta u_4^e = \frac{Q_4^x - \hat{K}_{41}u_1 - \hat{K}_{42}u_2 - \hat{K}_{43}u_3}{\hat{K}_{44}} \tag{39}$$

Similarly for the y-momentum equation

$$\delta v_4^e = \frac{Q_4^y - \hat{K}_{41}v_1 - \hat{K}_{42}v_2 - \hat{K}_{43}v_3}{\hat{K}_{44}} \tag{40}$$

At this point it is constructive to look at the structure of the matrices. Due to the choice of basis functions, for any element configuration several of the matrix components become zero.

$$\mathcal{K}_{14}^l = \mathcal{K}_{41}^l = \mathcal{K}_{24}^l = \mathcal{K}_{42}^l = \mathcal{K}_{34}^l = \mathcal{K}_{43}^l = 0 \tag{41}$$

$$\mathcal{C}_{44}^x = \mathcal{C}_{44}^y = 0 \tag{42}$$

As a result of Equation (42), the contribution of the pressure error (δp_4^e) in the element has no effect on the velocity error (δu_4^e). With this in mind the expanded approximate solution is:

$$\delta u_4^e = \frac{\mathcal{F}_4^x - \mathcal{C}_{41}^x p_1 - \mathcal{C}_{42}^x p_2 - \mathcal{C}_{43}^x p_3 - \hat{K}_{41}u_1 - \hat{K}_{42}u_2 - \hat{K}_{43}u_3}{\hat{K}_{44}} \tag{43}$$

$$\delta v_4^e = \frac{\mathcal{F}_4^y - \mathcal{C}_{41}^y p_1 - \mathcal{C}_{42}^y p_2 - \mathcal{C}_{43}^y p_3 - \hat{K}_{41}v_1 - \hat{K}_{42}v_2 - \hat{K}_{43}v_3}{\hat{K}_{44}} \tag{44}$$

The solutions to δu_4^e and δv_4^e can be used as indicators of how well the steady-state momentum equations are satisfied. A functional value of the error indicator over the domain can be expressed as,

$$\eta_x = \sum_{c=1}^{N} \Psi_4^e \delta v_4^e \tag{45}$$

$$\eta_y = \sum_{e=1}^{N} \Psi_4^e \delta v_4^e \tag{46}$$

With this error indicator a sufficient norm may be devised. In the present work an L_2 norm will be used,

$$L_2 = \sum_{e=1}^{N} \left[\int_{\Omega^e} (\eta_x^{e^2} + \eta_y^{e^2}) \, \mathrm{d}\Omega^e \right] \tag{47}$$

In the context of the element matrices we obtain,

$$L_2 = \sum_{e=1}^{N} [\delta u_4^e M_{44}^e \delta u_4^e + \delta v_4^e M_{44}^e \delta v_4^e] \tag{48}$$

In order to make this error independent of the size of the domain we simply divide by the area to obtain the L_2 per unit area. In order to obtain a graphically reasonable error indicator, a projection method is used to change from a space of functions ($\mathscr{S} - \mathscr{R}$) which can be represented by the basis functions Ψ_4^e where $e = 1, 2, 3 \ldots N$ ($N =$ number of elements) to a space ($\mathscr{R}$) which can be represented by the basis Ψ_i^e, where $i = 1, 2, 3$ and $e = 1, 2, 3 \ldots N$ ($N =$ number of elements), by minimizing the following functionals,

$$\Pi_x = \sum_{e=1}^{N} \left\{ \int_{\Omega^e} \left(\sum_{j=1}^{3} \Psi_j^e E_j^x - \Psi_4^e \delta u_4 \right)^2 \mathrm{d}\Omega^e \right\} \tag{49}$$

$$\Pi_y = \sum_{e=1}^{N} \left\{ \int_{\Omega^e} \left(\sum_{j=1}^{3} \Psi_j^e E_j^y - \Psi_4^e \delta u_4 \right)^2 \mathrm{d}\Omega^e \right\} \tag{50}$$

Finally, the errors in x and y are added together in a vector sense ($E_i = \sqrt{E_i^{x^2} + E_i^{y^2}}$) to obtain a scalar plot of the momentum error indicator. This quantity will be used later to develop contour plots of the momentum error in the domain.

NUMERICAL RESULTS

Two problems commonly seen in the literature were chosen as models — driven lid cavity, and flow over a backstep. The driven lid problem is a challenging problem due to the numerical singularity at the lid–cavity interface. Sohn *et al.* [4] suggest an integration by parts on the right hand side of the δp equation to help treat these geometric singular points. In this work no attempt is made to correct this singularity in any way. As a matter of fact, this singularity is a source of error which drives the error analysis for the cavity problem. The numerical results obtained for the cavity flows are compared with previous numerical results obtained by Ghia and Ghia [14]. Flow over a backstep is compared with the experimental results of Morgan *et al.* [15]. All solutions were continued until a velocity residual equation defined below was satisfied.

$$\frac{\int_\Omega |\bar{V}^{n+1} - \bar{V}^n|^2 \, \mathrm{d}\Omega}{\int_\Omega |\bar{V}^n|^2 \, \mathrm{d}\Omega} \leqslant 0.001 \tag{51}$$

All solutions were taken with a time step, Δt, of 0.01. Within each time step the numerical equations were solved using a conjugate gradient or bi-conjugate gradient iteration method.

Lid driven cavity flow

The geometry for the cavity problem is a unit square with zero velocity over all of the boundary except, for the top ($y = 1$) where the velocity is unity. The geometry for the cavity problem is shown in Figure 2. The Reynolds number varies as 100, 400, 1000 and 3200. These Reynolds numbers correspond to the set of numbers presented by Ghia and Ghia [14]. For each Reynolds number four different grid sizes will be used, 15×15, 20×20, 30×30 and 50×50. These grids were generated off of one 12-noded quadrilateral isoparametric element where the side nodes were shifted towards the corner nodes, as shown in Figure 3. This type of generation was used to ensure that each grid distribution can be consistently compared to the others in the solution and error sequence. The first judge of any error indicator is its approach to zero as the number of grid nodes are increased. In order to investigate this property for the indicator, we investigated the L2 error of the velocity as a function of the number of nodes for each mesh and Reynolds numbers. For the entire range of the grids

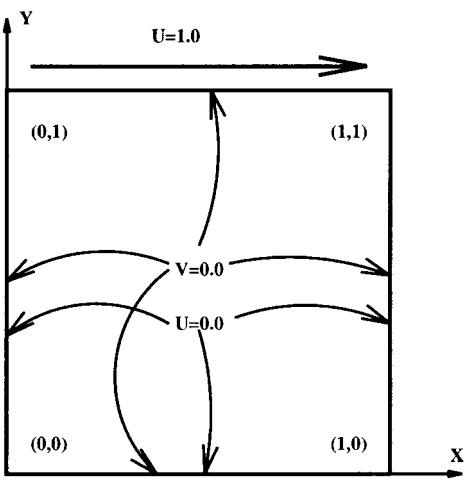

Figure 2. Geometry.

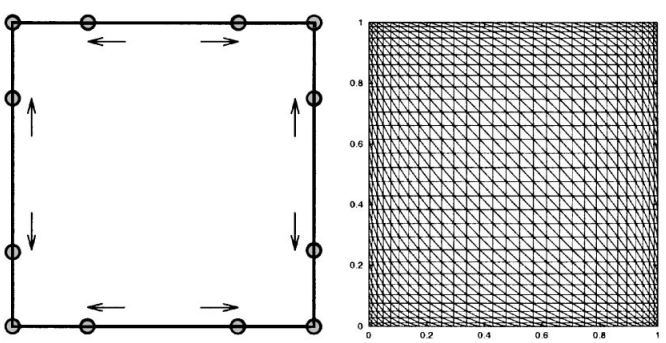

Figure 3. Twelve-noded isoparametric grid element and 30×30 resultant grid.

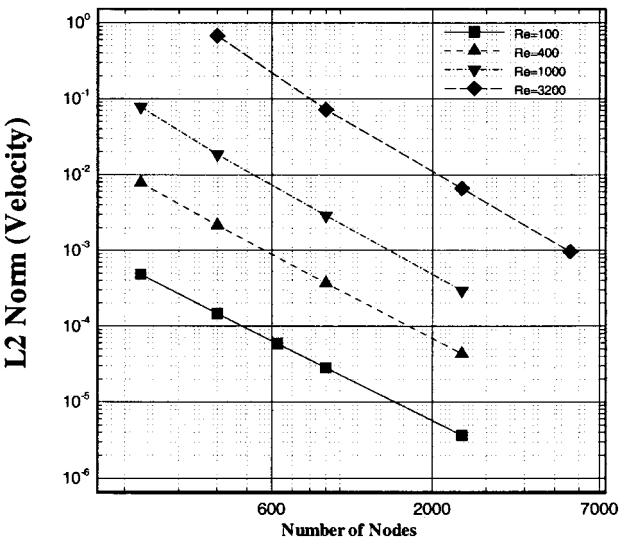

Figure 4. L2 error for all cavity cases.

and Reynolds numbers covered in the cavity problem, the L2 norm can be represented on one plot as shown in Figure 4. For every Reynolds number, the error indicator decreases as the number of nodes increase. This is exactly the behavior one would desire from an error indicator. Also, each Reynolds number case displays the same rate of convergence. Since the element types for all simulations are linear triangular, this is also an expected behavior. The next desirable feature of an error indicator is to display in which region of the domain the errors are greater than in others. For the cavity case, this behavior should be known ahead of time. The upper right and left of the cavity will display a singularity type of behavior. This should in fact be the major source of error in the domain. To investigate this, each Reynolds number will be considered and the projected error plots will be examined.

Reynolds number 100. For a Reynolds number of 100, the projected L2 error plot is shown in Figure 5. Several interesting features of this plot should be noted. First, the error is greatest in the upper left and right of the cavity. This is exactly what one should expect. In the absence of an exact solution the actual value of these L2 errors are as good as can be expected, especially since these errors are produced in a post-processing step. Another very interesting feature of this error plot is that these errors seem to propagate out into the cavity. For example, the error generated at the upper right hand corner of the cavity is actually convected down the cavity by the local velocity. The actual values of this L2 error is very small, as shown in the legend of the contour plot. Couple this with the fact that this plot is not smoothed, and one may conclude that this post-processing step can be of extreme value when attempting to find the source of possible errors in a simulation. For a Reynolds number of 100 this solution sequence is compared to the computational work of Ghia, shown in Figure 6.

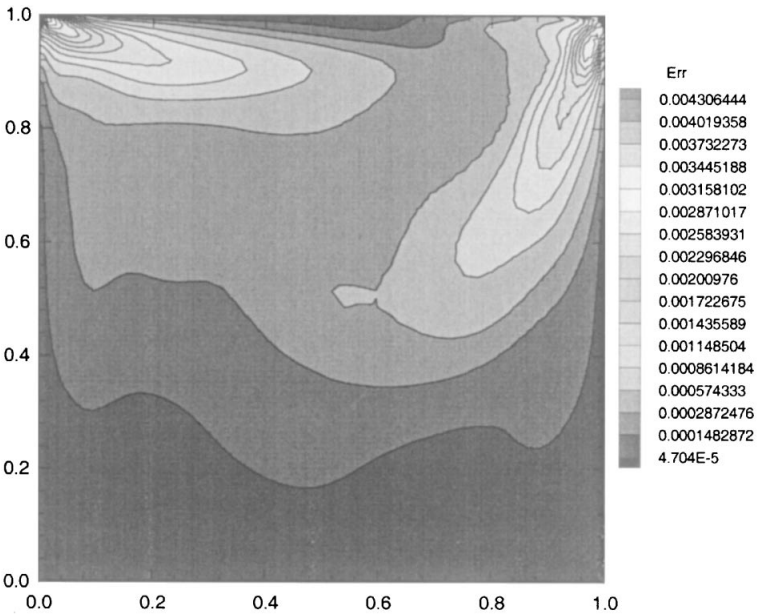

Figure 5. L2 error $Re = 100$ (50×50 grid).

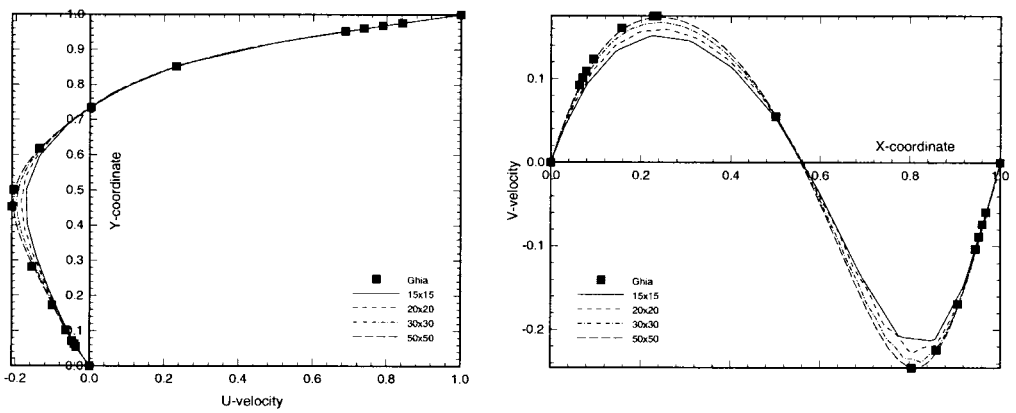

Figure 6. U and V velocity profiles compared to Ghia ($Re = 100$).

Reynolds number 400. For a Reynolds number of 400, the projected L2 error plot is shown in Figure 7. When this plot is compared to the Reynolds number 100 plot there are several differences that are apparent. First, the maximum value of the error is greater for the Reynolds number 400 case. More interesting is the appearance of the error contours. In the Reynolds number 400 case, the error is generated at the singularity points and is convected down into the cavity (for the upper right corner) or across the top of the cavity (for the upper right of the cavity). This behavior has been seen before by Oden *et al.* [16]. In their work an error

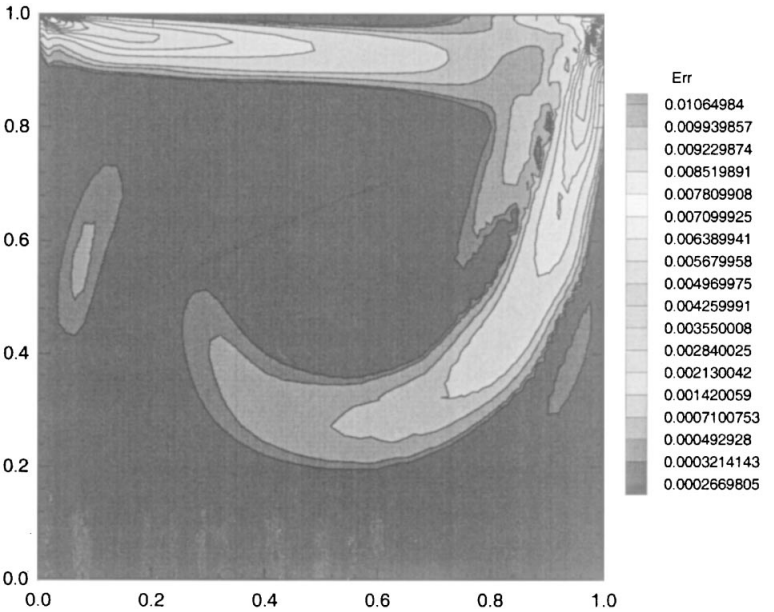

Figure 7. L2 error $Re = 400$ (50×50 grid).

equation was developed for a hyperbolic system of equations. Hence, the error equations have a convective characteristic in that an error produced in one area of the domain will be convected through the domain by the local velocity. Their work involved the development of an evolution of error equations to approximate the errors in the domain in space and time. In fact if one represents the errors in a solution by $\mathscr{E} = u_i^f - u_i^e$ where u_i^e is the exact solution (which does not exist in our case) and u_i^f is the finite element representation of the solution to the problem at hand, these terms may be used to develop an error equation.

$$0 = \frac{\partial u_i^e}{\partial t} + u_j^e \frac{\partial u_i^e}{\partial x_j} - f_i - \frac{1}{Re} \frac{\partial^2 u_i^e}{\partial x_j \partial x_j} \tag{52}$$

$$R = \frac{\partial u_i^f}{\partial t} + u_j^f \frac{\partial u_i^f}{\partial x_j} - f_i - \frac{1}{Re} \frac{\partial^2 u_i^f}{\partial x_j \partial x_j} \tag{53}$$

Where R is the finite element type residual. If the finite element representation of the solution satisfies the continuity constraint, i.e. $u_{i,1}^f = 0$. Then, subtracting one of these equations from the other, one may obtain,

$$R = \frac{\partial \mathscr{E}_i}{\partial t} + u_j^f \frac{\partial \mathscr{E}_i}{\partial x_j} + \mathscr{E}_j \frac{\partial u_i^e}{\partial x_j} - \frac{1}{Re} \frac{\partial^2 \mathscr{E}_i}{\partial x_j \partial x_j} \tag{54}$$

Although this equation will not be solved in any way or form, it is instructive to observe the way in which the error of a solution should perform. Here, the term $u_j^f [(\partial \mathscr{E}_i)/(\partial x_j)]$ is the finite element solution to the velocity, convecting the error through the domain. This behavior

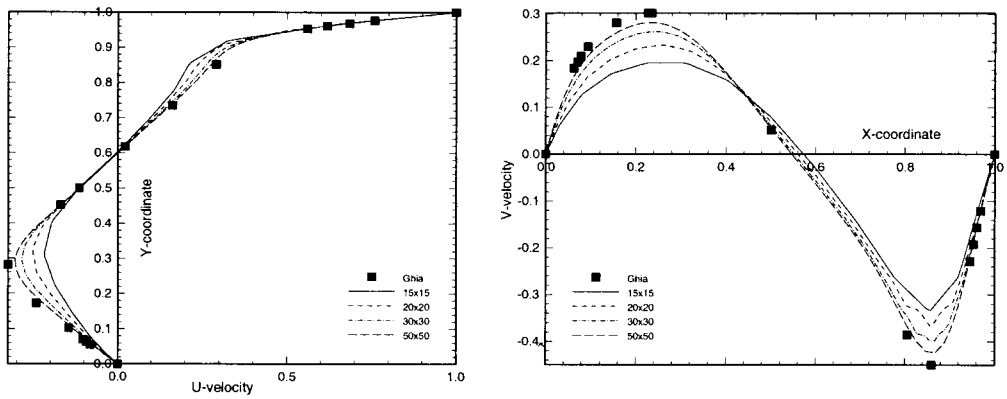

Figure 8. U and V velocity profiles compared to Ghia ($Re = 400$).

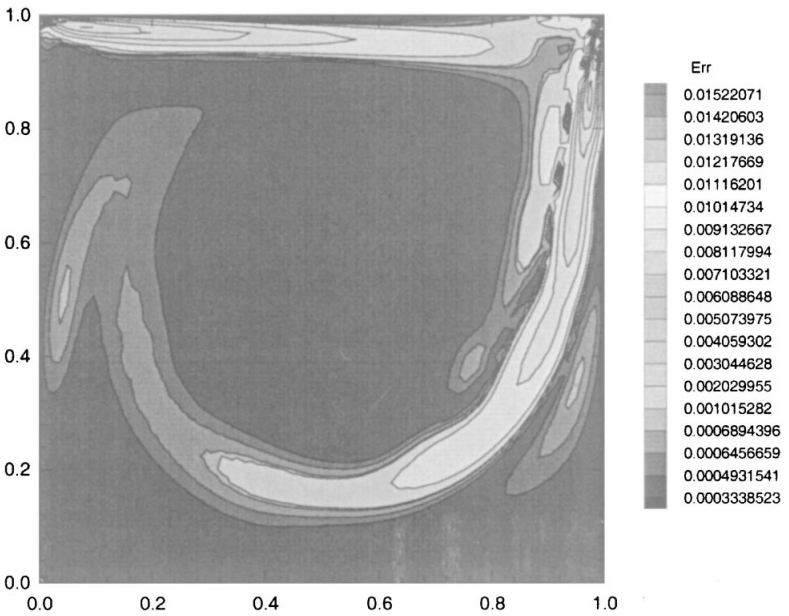

Figure 9. L2 error $Re = 1000$ (50×50 grid).

exist throughout all of the solutions in the present work. It is most apparent in the cavity solutions due to the existence of a high error at the upper corners. For this Reynolds number of 400 a comparison with the previous work of Ghia is shown in Figure 8.

Reynolds number 1000 & 3200. For a Reynolds number of 1000, the projected L2 error plot is shown in Figure 9. For this Reynolds number, the L2 error plot shows a behavior much like the 100 and 400 case. However, the errors are convected in a narrower band throughout

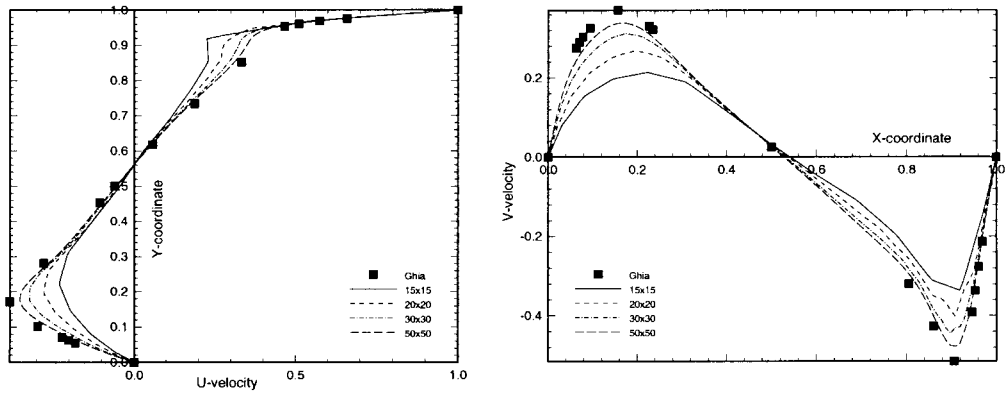

Figure 10. L2 error $Re = 3200$ (50×50 grid).

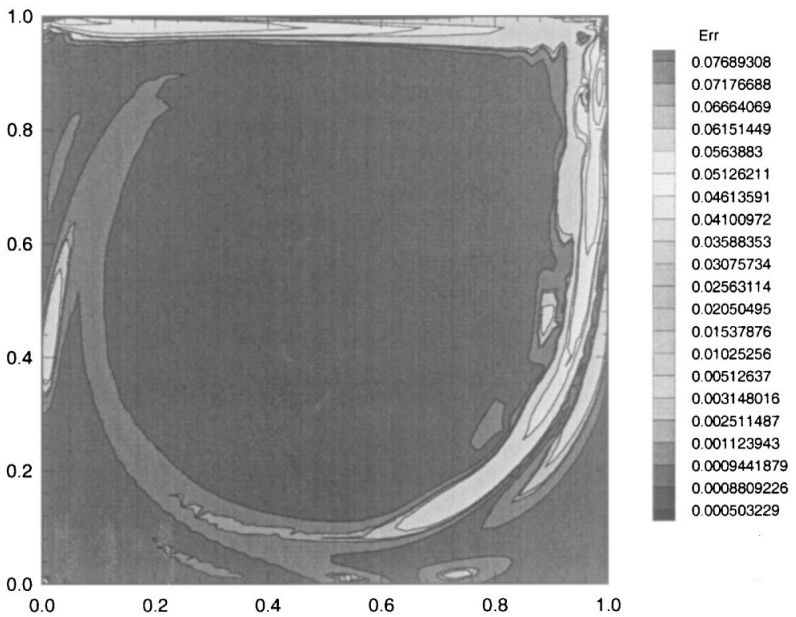

Figure 11. U and V velocity profiles compared to Ghia ($Re = 1000$).

the cavity. This is what one may expect due to the higher Reynolds number, the ratio of error convection to error diffusion will become large. This is exactly what can be seen by observing our error equation, Equation (54). As the Reynolds number increases, $1/Re[(\partial^2 \mathscr{E}_i)/(\partial x_j/\partial x_j)]$ decreases thereby allowing lower amounts of diffusion of the error. This narrowing of the convected portion of the error become more evident for the Reynolds number 3200 case, as shown in Figure 10. Comparison between the finite element solutions and that of Ghia is shown in Figures 11 and 12.

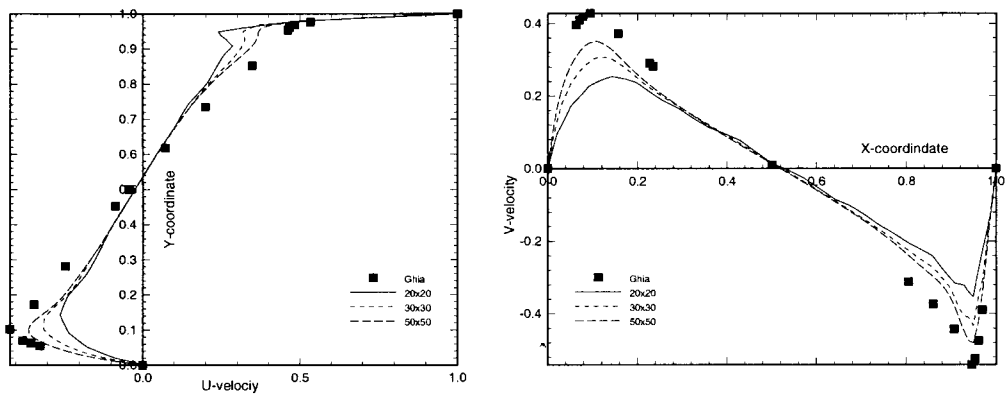

Figure 12. U and V velocity profiles compared to Ghia ($Re = 3200$).

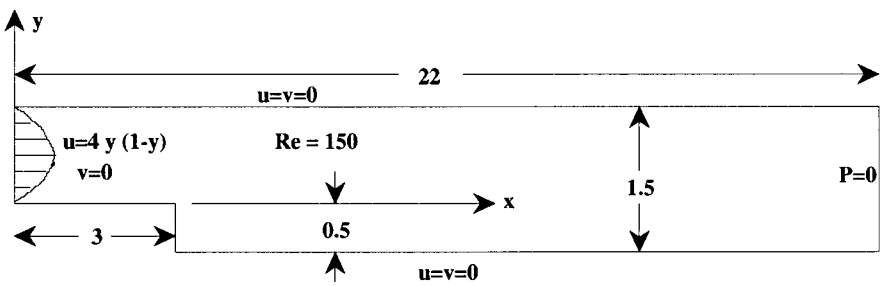

Figure 13. Geometry for backstep case.

FLOW OVER BACKSTEP

The next example is flow over a backstep. This geometry has also been chosen due to the availability of experimental data, the existence of a circulation zone, and lack of a numerical singularity [15]. The geometry chosen is case (iii) from Morgan *et al.* [15] and is shown in Figure 13. The Reynolds number of 150 is also chosen from case (iii).

The L2 error convergence plot of the solution process is shown in Figure 14. The convergence process does not follow a straight line on a log–log plot for this example. This occurs due to the fact that for a course mesh, the inlet boundary conditions cannot be met correctly. However, as the mesh becomes finer and finer, the inlet boundary condition approaches its required distribution. The L2 error contour plot is shown in Figure 15. This plot shows most of the error is produced at the corner of the backstep. There is a slight convection of this error down-stream of this corner, but nothing like that which occurred in the cavity problems.

In order to add validity to this numerical process we compare to the experimental results of Morgan *et al.* [15]. These comparisons are shown in Figures 16 and 17.

As in the cavity solutions, this comparison indicates the same trends. As the error indicator recedes, the difference between the numerical solution and experimental results also recedes: a pattern which would give any numerical analyst a basis for determining how well his solution is spatially converged.

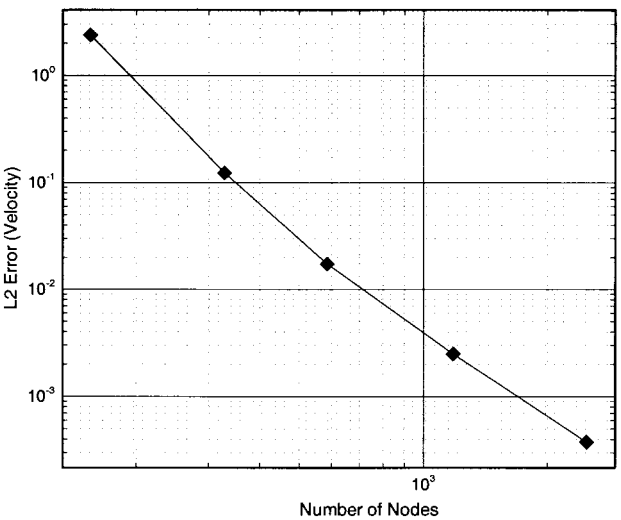

Figure 14. Convergence history for backstep case.

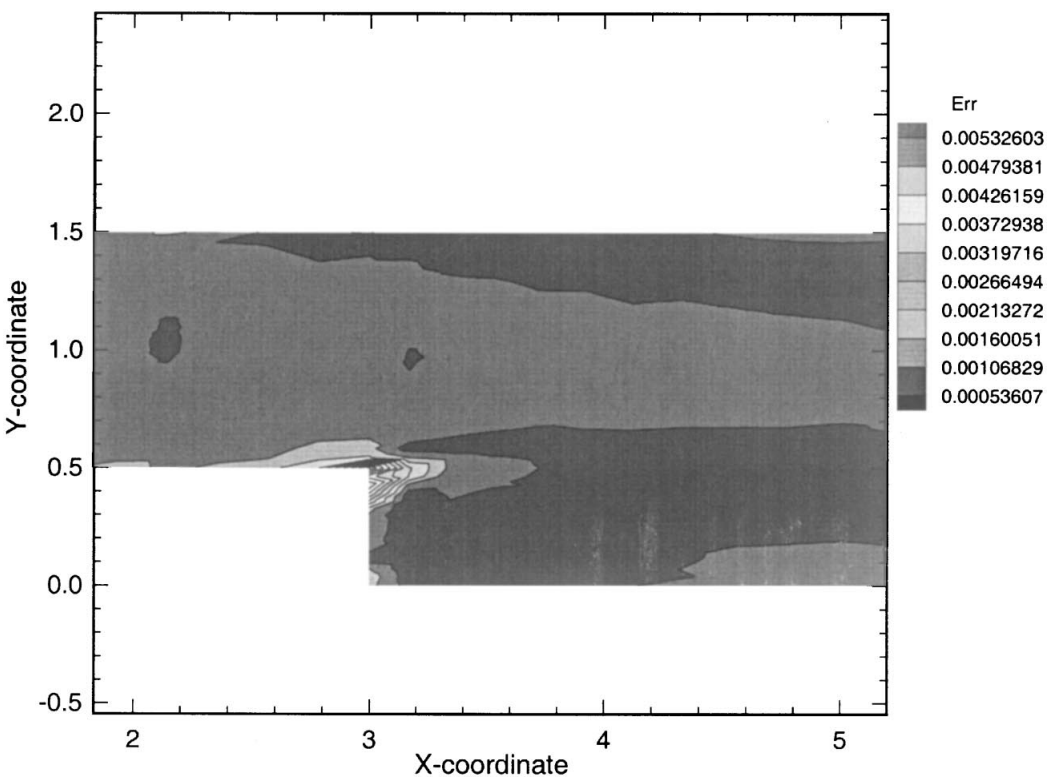

Figure 15. L2 error for backstep case.

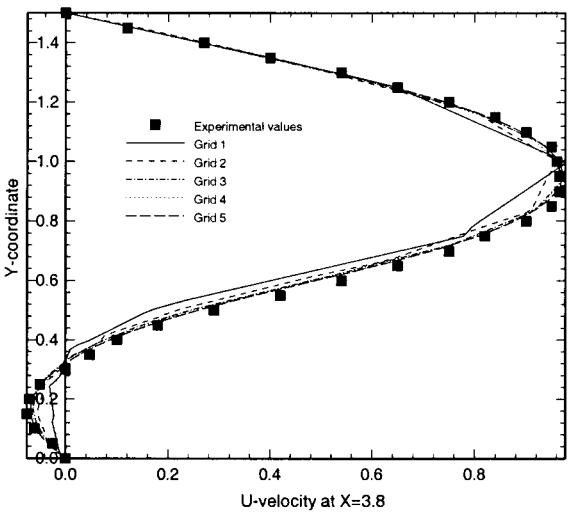

Figure 16. U velocity distribution at $x = 3.8$ behind the backstep.

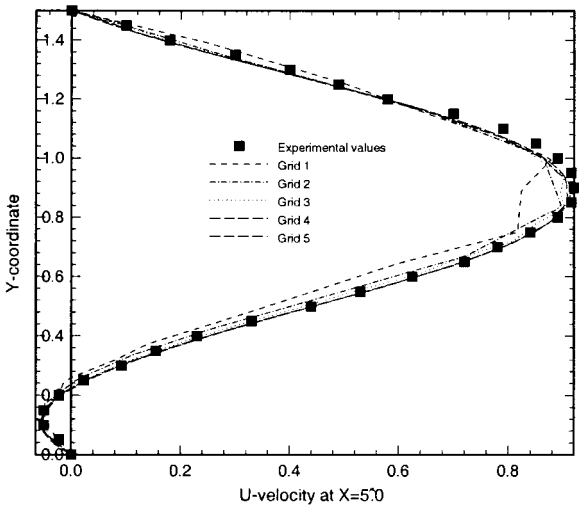

Figure 17. U velocity distribution at $x = 5.0$ behind the backstep.

CONCLUSIONS

A simple yet efficient method has been presented for determining an error estimator in incompressible fluid simulations. The error estimate is determined from the change in two levels of grid refinement, hence this indicator simply tells the user in what region and by how much the answer would change if he refined the grid in a specific manner. This error analysis is very efficient due to existence only in a post-processing step. Two examples were shown to

correlate very well with previously published information, i.e., as the error indicator became small; so too did the difference between the solution at hand and the data in the literature. Although the method was applied only to triangular elements, it should work equally as well with other types of elements.

Finally, as a result of this error analysis presented here, one should always consider sources and locations of possible error when producing a grid for a simulation. Convection-type equations will always have some convective component to their error equations. Hence, errors produced in a course grid region of the domain can actually convect down into a fine grid region of the domain.

REFERENCES

1. Comini G, Del Giudice S. Finite-element solution of the incompressible Navier–Stokes Equations. *Numerical Heat Transfer* 1982; **5**:463–478.
2. Comini G, Del Giudice S. A ($k - \varepsilon$) model of turbulent flow. *Numerical Heat Transfer* 1985; **8**:133–147.
3. Kim YM, Chung TJ. Finite element analysis of turbulent diffusion flames. *AIAA Journal* 1989; **27**(3):330–339.
4. Sohn JL, Kim YM, Chung TJ. Finite element solvers for incompressible fluid flows and heat transfer. In *Finite Element Analysis in Fluids*, Proceeding of the Seventh International Conference on Finite Element Methods in Flow Problem, Chung TJ, Karr GR (eds). University of Alabama Press: Huntsville, 1989; 880–885.
5. Carey GF, Oden JT. *Finite Element—A Second Course*. Prentice Hall: Englewood Cliffs, NJ, 1983.
6. Reddy JN. *Applied Functional Analysis and Variational Methods in Engineering*. McGraw Hill, 1986.
7. Dukowicz JK, Dvinsky AS. Approximate factorization as a high order splitting for the implicit incompressible flow equations. *Journal of Computational Physics* 1992; **102**:336–347.
8. Gresho PM, Chan ST, Christon MA, Hindmarsh AC. A little more on stabilized Q_1 Q_t for transient viscous incompressible flow. *International Journal for Numerical Methods in Fluids* 1995; **21**:837–856.
9. Zienkiewicz OC, De Gago SR, Kelly DW. The hierarchical concept in finite element analysis. In *Advances and Trends in Structural and Solid Mechanics*, Symposium on Advances and Trends in Structural and Solid Mechanics, Noor AK, Housner JM (eds). Pergamon Press: Oxford, U.K., 1983; 53–65.
10. Kelly DW, De Gago SR, Zienkiewicz OC, Babuska I. A posteriori error analysis and adaptive processes in the finite element method: Part I—Error analysis. *International Journal for Numerical Methods in Engineering* 1983; **19**:1593–1619.
11. Kelly DW, De Gago SR, Zienkiewicz OC, Babuska I. A posteriori error analysis and adaptive processes in the finite element method: Part 2—Adaptive mesh refinement. *International Journal for Numerical Methods in Engineering* 1983; **19**:1621–1256.
12. Reddy JN. *An Introduction to the Finite Element Method*. McGraw Hill: New York, 1984.
13. Patankar SV. *Numerical Heat Transfer and Fluid Flow*. Hemisphere: New York, 1980.
14. Ghia KN, Ghia U. Elliptic systems: finite-difference method III. *Handbook of Numerical Heat Transfer*, Minkowycz WJ, Sparrow EM, Schneider GE, Pletcher RH (eds). John Wiley and Sons: New York, 1988; 293–346.
15. Morgan K, Periaux J, Thomasset F (eds). *Analysis of Laminar Flow Over a Backward Facing Step*. Friedr. Vieweg and Sohn: Braunschweig, Wiesbaden, Germany, 1984.
16. Oden JT, Strouboulis T, Bass JM. Paradigmatic error calculations for adaptive finite element approximations of convective dominated flows. *Recent Developments in Computational Fluid Dynamics*, *ASME AMD* 1988; **95**:147–162.

